Structural characterization of biomedical Co-Cr-Mo components produced by Direct Metal Laser Sintering.

note finali coverpage

(Article begins on next page)

17 April 2024

Structural characterization of biomedical Co-Cr-Mo components produced by Direct Metal Laser Sintering

G. Barucca [a,*], E. Santecchia [a], G. Majni [a], E. Girardin [b], E. Bassoli [c], L. Denti [c], A. Gatto [c], L. Iuliano [d], T. Moskalewicz [e], P. Mengucci [a]

[a] SIMAU, Università Politecnica delle Marche, via Brecce Bianche, 60131 Ancona, Italy.

[b] DISCO, Università Politecnica delle Marche, via Brecce Bianche, 60131 Ancona, Italy.

[c] DIMeC, University of Modena and Reggio Emilia, via Vignolese 905/B, Modena 41125, Italy.

[d] DISPEA, Politecnico di Torino, C.so Duca degli Abruzzi 24, 10129 Torino, Italy.

[e] Faculty of Metals Engineering and Industrial Computer Science, AGH University of Science and Technology, Al. Mickiewicza 30, 30-059 Kraków, Poland.

[*] Corresponding author: SIMAU, Università Politecnica delle Marche, via Brecce Bianche, 60131 Ancona, Italy. Tel.: +39 071 2204754; fax: +39 071 2204729.

E-mail address: g.barucca@univpm.it (G. Barucca).

18 **ABSTRACT**

19 Direct Metal Laser Sintering (DMLS) is a technique to manufacture complex functional

20 mechanical parts from a computer-aided design (CAD) model. Usually, the mechanical

21 components produced by this procedure show higher residual porosity and poorer mechanical

22 properties than those obtained by conventional manufacturing techniques.

23 In this work, a Co-Cr-Mo alloy produced by DMLS with a composition suitable for biomedical

24 applications was submitted to hardness measurements and structural characterisation. The alloy

25 showed a hardness value remarkably higher than those commonly obtained for the same cast or

26 wrought alloys. In order to clarify the origin of this unexpected result, the samples microstructure

27 was investigated by X-ray diffraction (XRD), electron microscopy (SEM and TEM) and energy

28 dispersive microanalysis (EDX). For the first time, a homogeneous microstructure comprised of

29 an intricate network of thin ε (hcp)-lamellae distributed inside a γ (fcc) phase was observed. The

30 ε-lamellae grown on the $\{111\}_\gamma$ planes limit the dislocation slip inside the γ (fcc) phase, causing

31 the measured hardness increase. The results suggest possible innovative applications of the

32 DMLS technique to the production of mechanical parts in the medical and dental fields.

33

34

37

1. INTRODUCTION

Nowadays, a new class of manufacturing methods are becoming increasingly important for the production of biomedical devices. Among them, novel methods based on additive manufacturing (AM), assisted by computer-aided design/computer-aided manufacturing (CAD/CAM), allow the production of intricate mechanical parts [1-4].

Direct metal laser sintering (DMLS) is an AM process that uses the heat of a solid state laser to sinter metal powder particles [5]. In this case, a distribution mechanism pre-places successive layers of powder on a suitable substrate, while a laser beam controlled by a scanning system locally sinters the powder in accordance with the CAD model [6]. This technology, like other AM procedures, is highly rewarding in medicine where a high degree of personalization is required [7-9]. Prosthetic applications are particularly well suited for processing by means of DMLS due to their complex geometry, low volume and strong individualization [10]. Furthermore, the manufacturing of multiple unique parts in a single production run enables extensive customization with a strong reduction of manual operation leading to higher repeatability and good savings in money and delivery times.

Cobalt-based alloys were extensively used in cast and hard facing forms over the past twenty years because of their corrosion and wear resistance, biocompatibility and excellent strength and toughness at high temperature [11]. Typical applications of the Co-based alloys involved both the biomedical and the metallurgical fields [12, 13].

From a structural point of view, cobalt is characterized by a ε (hcp) low temperature phase and a γ (fcc) phase at higher temperature. The addition of chromium improves the corrosion and the oxidation resistance of the alloy, as well as its hardness, ductility and wear resistance through

60 carbide formation. Molybdenum improves the corrosion resistance and acts as a solid-solution

61 strengthener by forming the Co_3Mo (hcp) intermetallic compound [14].

62 Cast alloys with a Cr content ranging from 19 wt% to 30 wt% and a Mo content in the range 5-

63 10 wt% were considered for biomedical applications and for many years these compositions

64 were used to produce medical implants such as hips, knees, ankles and bone plates [15].

65 Although in the past few years, several AM techniques were applied to produce biocompatible

66 Co-based alloys, only in few cases a deep microstructural characterisation of the sintered

67 components were performed. In particular, Gaytan et al. reported on the microstructure and the

68 mechanical properties of Co-based prototypes produced by electron beam melting. In this study,

69 they found high hardness values attributed to the formation of an ordinate array of metal carbides

70 [16]. Meacock et al. investigated the microstructure and the mechanical properties of a

71 biomedical Co-Cr-Mo alloy produced by laser powder microdeposition [17]. They observed a

72 homogenous microstructure comprised of fine cellular dendrites and measured an average

73 hardness value of 460 HV_{02}, well higher than the typical values obtained by other fabrication

74 processes. From these results, they concluded that the fine morphology is responsible of the

75 significantly increased hardness value.

76 Few other papers deal with the possibility of realizing medical parts of a Co-Cr-Mo alloy by the

77 DMLS technique, but it is worth to note that none of them reports on the correlation of the

78 samples microstructure to the mechanical properties of the final components as well as detailed

79 transmission electron microscopy analyses [19-21].

80 The mechanical properties of the sintered components are strictly linked to the samples

81 microstructure and are one of the major aspects connected to the practical applications of the AM

82 procedures. Usually, objects produced by metal powder sintering show poorer mechanical

83 properties than those produced by conventional procedures. This behaviour is mainly due to the

84 fact that DMLS, depending on the laser energy density employed, involves a partial or total

85 melting of the powder. Therefore, the products made by DMLS could show high surface

86 roughness, porosity (in certain cases even lack of densification), heterogeneous microstructure

87 and thermal residual stresses that may give rise to poor mechanical properties [22].

88 In this paper, metallic components of a biocompatible Co-Cr-Mo alloy produced by the DMLS

89 technique were deeply investigated in order to correlate their hardness behaviour to the

90 corresponding microstructure. To this aim, hardness measurements, X ray diffraction (XRD)

91 analysis, electron microscopy (SEM, TEM) observations and energy dispersive microanalysis

92 (EDX) were performed on the samples. Results evidenced a surprisingly high hardness value of

93 the investigated Co-Cr-Mo alloy in comparison of the hardness values commonly reported in

94 literature for similar compositions. This unexpected result was attributed to the peculiar

95 microstructure observed in the analysed samples, that, to our knowledge, was never reported

96 before.

97

98 **2. MATERIALS AND METHODS**

99 *2.1 Material composition and sintering parameters*

100 Specimens were prepared by direct metal laser sintering using a Yb (ytterbium) fiber laser

101 system (EOSINT-M270) operating with the standard deposition parameters reported in Table1.

102 **Table 1**

103   Parameters used for DMLS

laser power	200W
laser spot diameter	0.200 mm
Scan speed	up to 7.0 m/s
Building speed	2-20 mm^3/s
Layer thickness	0.020 mm
Protective atmosphere	max 1.5% oxygen

104

105 A Co-Cr-Mo alloy powder (EOS Cobalt/Chrome SP2) with the nominal composition (in wt%)

106 Co 63.8, Cr 24.7, Mo 5.1, W 5.4 , Si 1.0, was used as raw material. The powder is free of Ni, Be

107 and Cd according to EN ISO 22674. The nominal composition was provided by the manufacturer

108 (EOS GmbH Electro Optical Systems). The powder is the EOS Cobalt/Chrome SP2 cobalt based

109 metal ceramic alloy intended for production of Porcelain-Fused to Metal (PFM) dental

110 restorations (crowns, bridges, etc.) in EOSINT M 270 Standard installation mode. The powder is

111 class IIa medical device in accordance with annex IX rule 8 of the MDD 93/42/EEC.

112 Composition corresponds to "type 4" CoCr dental material according to EN ISO 22674.

113 Rectangular parallelepipeds with size 250 mm x 4 mm and a thickness of 6 mm were sintered by

114 using the parameters reported in Table 1. In order to minimize anisotropy, each layer was built

115 with the laser scanning along a specific direction. Layer-by-layer the scanning direction was

116 rotated by 25° with respect to the previous one.

117

118 *2.2 Hardness measurements*

119 Hardness tests were performed on the sintered samples using the Rockwell scale C

120 (specifications ISO 4498 : Sintered metal materials, excluding hard metals - Determination of

121 apparent hardness and microhardness). Measurements were obtained averaging five indentations

122 following ISO 6508: Rockwell hardness test.

123

124 *2.3 Structural characterisation*

125 Structural and microstructural characterizations were carried out by X-ray diffraction (XRD),

126 scanning (SEM) and transmission (TEM) electron microscopy techniques.

127 XRD measurements were performed by a Bruker D8 Advance diffractometer operating with a

128 Cu-Kα radiation source at V= 40kV and I= 40 mA in the angular range 2θ=10 - 90°.

129 SEM analyses were carried out by a ZEISS SUPRA 40 microscope equipped with a Bruker

130 Quantax energy dispersive X-ray microanalysis (EDX). Observations were performed on both

131 the as-received metallic powder and cross-sectioned sintered samples. Before observations,

132 samples surfaces were prepared using a conventional metallographic procedure and

133 electrochemically etched in the following conditions: HCl 0.1 M, 2V, 2 min.

134 TEM analyses were carried out by a Philips CM200 electron microscope operating at 200 kV

135 and by a JEOL JEM-2010 ARP microscope equipped with an Oxford Inca energy dispersive X-

136 ray microanalysis (EDX). For TEM observations, samples were prepared by the conventional

137 thinning procedure consisting of mechanical polishing by grinding papers, diamond pastes and a

138 dimple grinder. Final thinning was carried out by an ion beam system (Gatan PIPS) using Ar

139 ions at 5 kV.

140

141 **3. RESULTS**

142 *3.1 Hardness*

143 The average Rockwell C hardness (HRC) value measured for the laser sintered samples is 47

144 HRC, a very high value considering that the usual range for cast Co-Cr-Mo alloys is from 25 to

145 35 HRC.

146

147 *3.2 X-ray diffraction (XRD)*

148 X-ray diffraction measurements were performed on both the Co-Cr-Mo powder used as raw

149 material for the DMLS process and on the different regions of the sintered samples (Fig. 1).
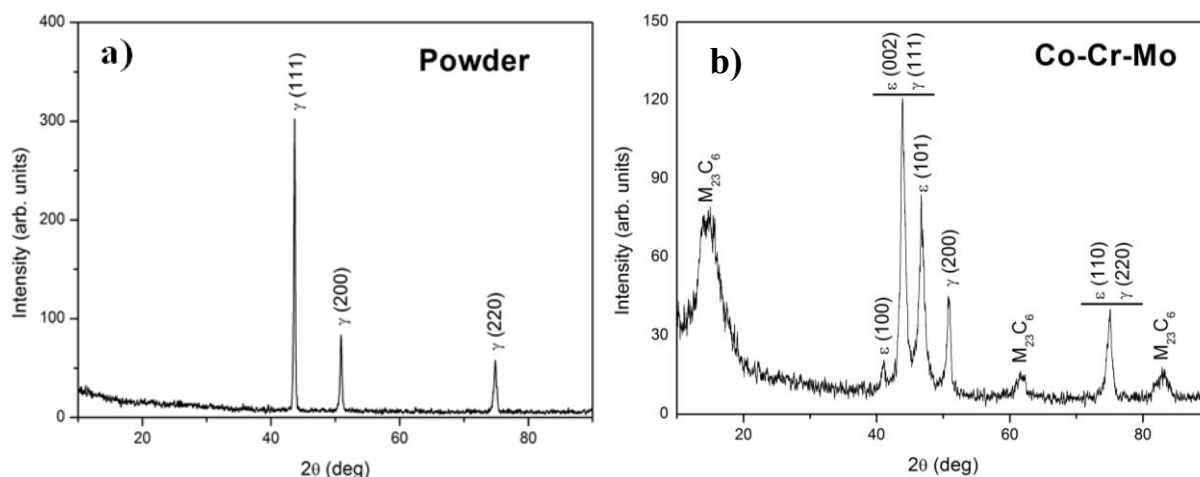
150 **Fig. 1.** *X-ray diffraction patterns: a) as-received metallic powder; b) sintered sample.*

151

152 Fig. 1a reports the XRD pattern of the as-received metallic powder. All the visible peaks can be

153 attributed to the cubic cobalt phase, commonly referred to as γ phase. The γ phase has a face

154 centred cubic (fcc) lattice with a nominal parameter a=0.35447 nm (ICDD card n. 15-806). For

155 the alloy under study, the best fit performed by using the three diffraction peaks of Fig. 1a

156 provides a lattice parameter value a=0.3586 nm, in close agreement with the values reported in

157 literature for alloys of similar composition [23].

8

158 The XRD pattern of the sintered sample is shown in Fig. 1b. The most intense and well-defined

159 peaks are a result of the simultaneous presence of both γ and ε cobalt phases, as indicated in Fig.

160 1b where each diffraction peak is indexed with the name of the corresponding Co phase. A

161 double indexation is reported for the most intense peak at $2\theta=43.94°$ and the peak at $2\theta=75.09°$

162 because of the superposition of the reflections due to the ε and γ phases. The ε phase has a

163 hexagonal close packed (hcp) lattice with nominal parameters a=0.25031 nm and c=0.40605 nm

164 (ICDD card n. 5-727). By using the ε (100) and ε (101) peaks of the XRD pattern shown in Fig.

165 1b, the lattice parameters of the hexagonal ε phase formed in our alloy were determined to be

166 a=0.2539 nm and c=0.4122 nm with a c/a ratio of 1.623. The lattice parameter of the fcc γ phase

167 formed in the sintered sample evaluated by the γ (200) peak of Fig. 1b is a=0.3589 nm. Also in

168 this case, the calculated lattice parameters for the ε and γ phases formed in our alloy are in close

169 agreement with those reported in literature for similar compositions [23].

170 In order to estimate the volume fraction of the hcp and fcc cobalt phases in the sintered sample,

171 the integrated intensities of the γ (200) and ε (101) peaks were used. The quantitative

172 determination, performed by using the method of Sage and Gillaud [24], resulted in an ε-phase

173 volume fraction $f_{hcp}=0.49\pm0.03$.

174 In addition to the ε and γ peaks in Fig. 1b, three broad peaks attributable to metals carbides are

175 also visible. These latter peaks generically indexed as $M_{23}C_6$ (M=Cr, Co, Mo, W) are due to

176 metal carbides having the cubic structure of the $Cr_{23}C_6$ compound (ICDD card n. 35-783).

177

178 *3.3 Scanning electron microscopy (SEM) and microanalysis (EDX)*

179 Scanning electron microscopy observations were performed on the as-received powder and on

180 the sintered samples. Particles forming the metallic powder are shown in Fig. 2.

181   From the SEM images the average size of the spherical particles were evaluated. Measurements

182   were performed by averaging the data obtained from different areas of the samples. Results

183   showed that the size of the particles ranges from 4 to 80 μm.
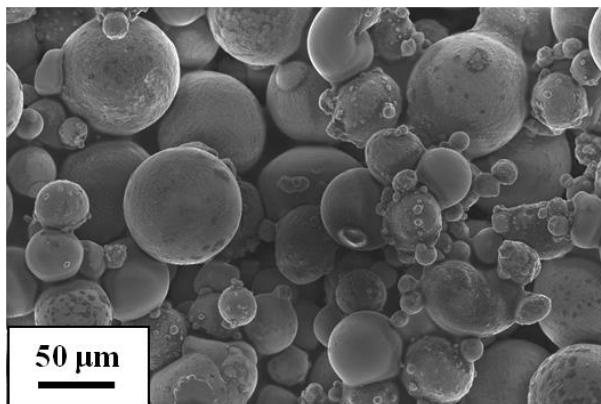
184   **Fig. 2.** *SEM image of the as-received metallic powder.*

185   EDX analysis performed on the powder showed a chemical composition in agreement with the

186   nominal composition of the alloy reported above. In Table 2 the experimental values obtained

187   from the EDX analyses performed on the powder and on the sintered sample are reported.

188

189   **Table 2**

190   Experimental results of the EDX microanalysis performed on both the powder and the sintered

191   sample.

Element	Powder (wt%)	Sintered sample (wt%)
Co	62	63
Cr	26	26
Mo	5	6
W	4	4
Si	1	1

192

193   It is worth to note that the average composition of the powder and the sintered sample is almost

194   the same, as can be inferred from Table 2.

195   The inner structure of the sintered samples, as observed by SEM, is shown in Fig. 3. Samples

196   were sectioned parallel to the laser beam direction, and SEM observations were performed after

197   a metallographic preparation of the surfaces followed by an electrochemical etching. The lines

198   separating the different weld pools produced by the laser scan on each layer are evidenced by

199   arrows in the image taken at low magnification, Fig. 3a.
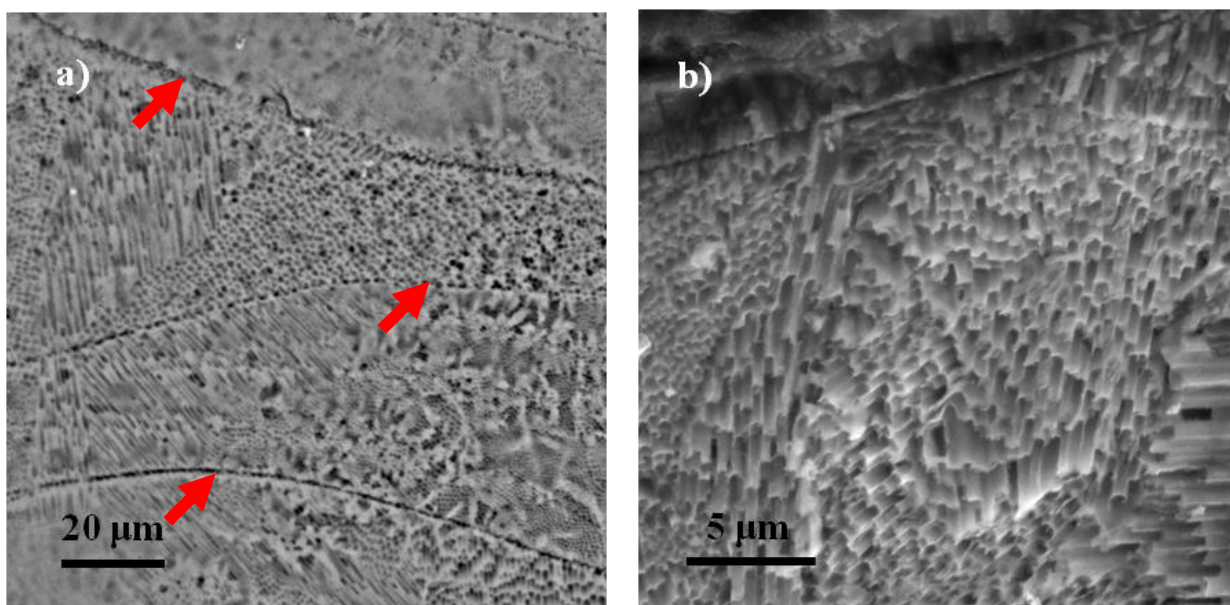
200   **Fig. 3** *SEM images of the sintered samples. a) low magnification: lines separating different weld*

201   *pools are arrowed; b) high magnification.*

202

203   Observations performed at higher magnification allow to evidence the presence of an extremely

204   fine microstructure inside a single pool, Fig. 3b. Columnar structures, with diameters ranging

205   from 300 to 400 nm and heights from 4 to 8 μm, grow inside the matrix in form of domains. The

206   orientation of the columns is the same inside a single domain while it changes from one domain

207   to the other. In order to estimate the area fraction occupied by the columnar structures relative to

208   the matrix, several SEM images were processed by using an image analysis software [25]. An

209   area fraction of 45±5% was provided by software. This value, as a rough approximation, can be

210   considered as the volume fraction of the columnar structures relative to the rest of the sample.

211

212   *3.4 Transmission electron microscopy (TEM) and microanalysis (EDX)*

213   TEM observations of the sintered samples confirm the presence of the two ε and γ cobalt phases.

214   The ε phase forms as small lamellae inside the γ phase. The thickness of the ε phase lamellae is

215   1-2 nm, but in some cases, they tend to aggregate in the same region of the sample forming

216   alternate structures of ε and γ phases with lateral dimensions of up to 400 nm.

217
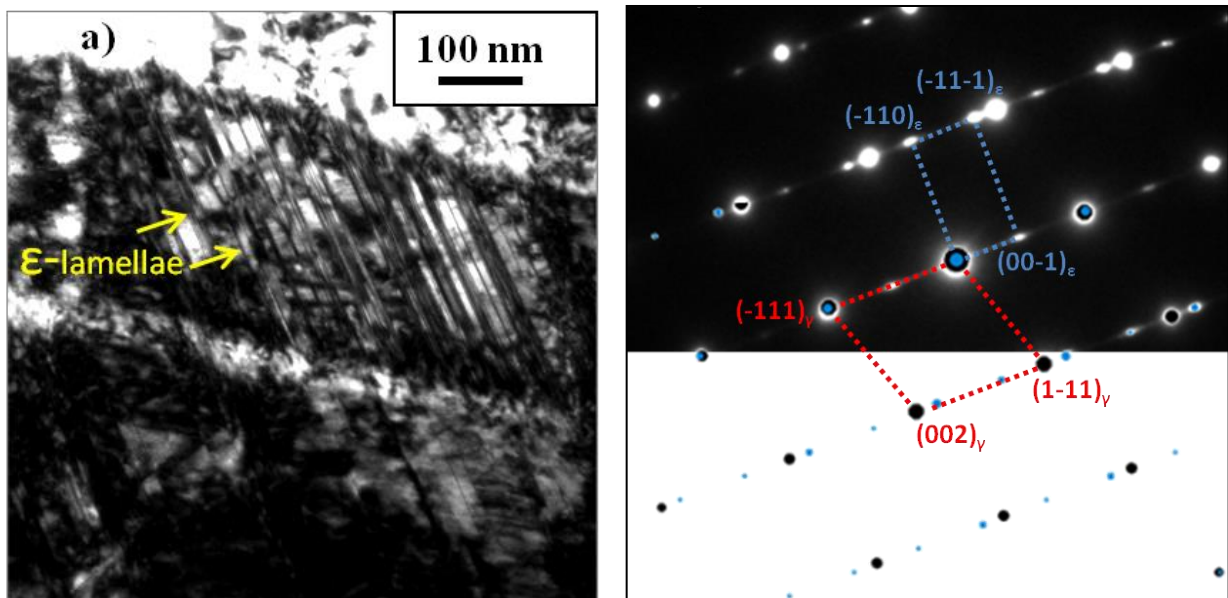
218   **Fig. 4.** *Sintered sample: a) TEM bright field image of the ε lamellae inside the γ phase*

219   *(arrowed); b) SAD pattern taken in the same area in <110>γ zone axis orientation (upper part)*

220   *and corresponding software simulation (lower part). In red is indicated the cell of the γ-Cobalt*

221   *phase and in blue the cell of the ε-Cobalt phase.*

222

223   In Fig. 4a, taken in $<110>_\gamma$ zone axis orientation, the lamellar structure is clearly visible. The

224   lamellae are parallel to each other, and the distance between them is not constant. Considering

225   the ensemble of these lamellae, it is possible to envisage one of the columnar structures visible in

226   the SEM images. The corresponding selected area diffraction (SAD) pattern is reported in the

227   upper part of Fig. 4b while its simulation performed with the CrystalKitX software [26] is shown

228   in the lower part of Fig. 4b. The remarkable agreement between the simulated pattern and the

229   experimental one is evident. The most intense spots visible in Fig. 4b (top) are a result of the fcc

230   γ-phase (red cell) while the smaller ones are a result of the hcp ε-phase (blue cell). The geometry

231   of the spot distribution in the SAD pattern of Fig. 4b (top) reveals that the ε lamellae form with

232   the following orientation relationships with the γ matrix:

233 $\{001\}_\varepsilon$ // $\{111\}_\gamma$

234 $<100>_\varepsilon$ // $<1\text{-}10>_\gamma$

235   Furthermore, as can be observed in Fig. 4b (top), the spots of the ε phase are streaked in direction

236   of the $\{111\}_\gamma$ spots indicating that the lamellae grow on the $\{111\}_\gamma$ lattice planes and have a

237   small thickness in the $<111>_\gamma$ lattice direction.

238   In order to investigate the spatial distribution of the hcp lamellae in greater details, TEM

239   observations were also performed in the $<111>_\gamma$ zone axis orientation.
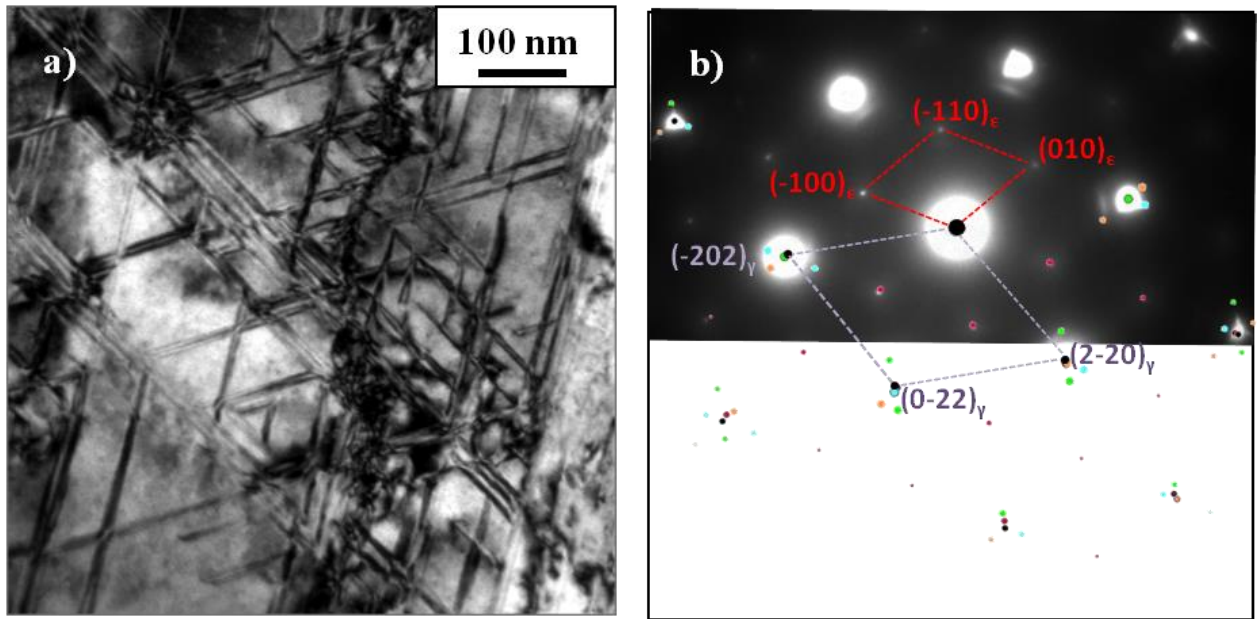
Fig. 5. *Sintered sample: a) bright field TEM image taken in <111>γ zone axis orientation; b) corresponding SAD pattern (upper part) and software simulation (lower part). In red is indicated the cell of the ε-Cobalt phase in one of the four possible orientations on the {111}γ lattice planes, and in violet the cell of the γ-Cobalt phase.*

A bright field image of the sample in this orientation is shown in Fig. 5a. Lamellae and stacking faults lying on different {111}γ lattice planes are visible and form an intricate network. The corresponding SAD pattern, with the simulation performed by the CrystalKitX software, are shown in the upper and lower part of Fig. 5b, respectively. The SAD pattern was simulated considering the four possible orientations of the ε phase on the {111}γ lattice planes. Different colours correspond to different orientations. In particular the diffraction spots corresponding to the $(001)_\varepsilon$ // $(111)_\gamma$ orientation were indexed in Fig. 5b and indicated with the red cell.

It must be stressed that all the SAD patterns, taken even in other orientations, never showed the presence of twins reflections (1/3 <hkl>), although at a first glance the ε lamellae could be confused with microtwins.

14

255 TEM observations performed on the sintered samples also revealed the presence of small

256 quantities of precipitates uniformly distributed. Precipitates, visible as dark dots inside the matrix

257 in Fig. 6, have a spherical or elliptical shape with size ranging from 50 to 300 nm.
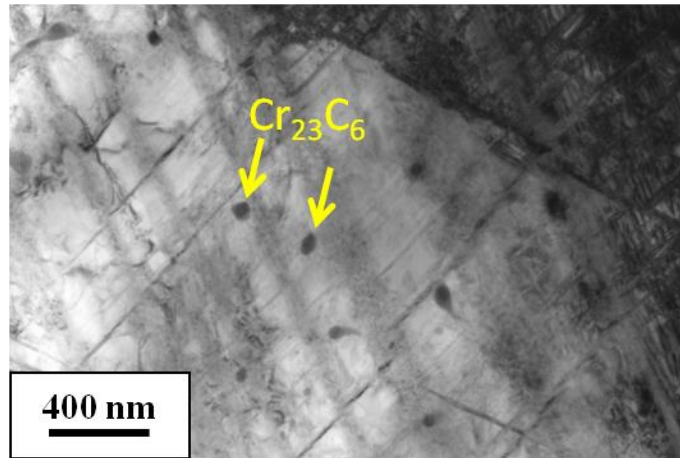
258 **Fig. 6.** *TEM bright field image of the sintered sample showing the presence of some metal*

259 *carbides (arrowed).*

260

261 In order to investigate the chemical composition of these precipitates, EDX measurements were

262 performed. Results show an increase of the Cr, W and Mo content in the precipitates with respect

263 to the matrix, while the precipitates composition remains almost the same independently of their

264 shape, Table 3. The crystallographic nature of the precipitates was investigated by the SAD

265 technique. Results are compatible with the presence of a phase having the $Cr_{23}C_6$ lattice

266 structure.

267 **Table 3**

268 Experimental results of the EDX measurements performed on both the matrix and the

269 precipitates.

Element	Matrix (wt%)	Precipitates (wt%)
Co	63	52
Cr	24	26
Mo	5	11
W	6	10
Si	1	1

270

271 **4. DISCUSSION**

272 The hardness values of the laser sintered samples are surprisingly high, considering the method

273 used for their realization. Generally, components produced by an additive manufacturing

274 technique, such as the Direct Laser Metal Sintering procedure used in this work, can be affected

275 by residual porosity and show poorer mechanical properties than those obtained by traditional

276 manufacturing techniques [22]. In our case, however, hardness results to be remarkably high,

277 even if compared to the same cast or wrought alloy. The explanation of this result is linked to the

278 inner structure of the samples, as will be discussed below. Furthermore, it must be stressed that

279 hardness is only one of the mechanical properties playing an important role in material selection

280 for application in the human body [12]. Other quantities such as tensile strength, Young's

281 modulus and elongation must be considered when the application range of a biomaterial is

282 involved. On the other hand, Murr et al. demonstrated the possibility to set the Young's modulus

283 of femoral component constituted of a Co-29Cr-6Mo alloy by opportunely developing mesh and

16

284   foam implant prototypes produced by an additive manufacturing technique [27]. This means that

285   the implant design influences also its final mechanical properties.

286   X-ray diffraction results show a phase transformation connected to the laser treatment. In

287   particular, while the powder is exclusively composed of the γ (fcc) cobalt phase, the sintered

288   sample contains both the γ (fcc) and ε (hcp) phases. Cobalt-based alloys undergo an fcc $\leftrightarrow$ hcp

289   martensitic transformation. The equilibrium temperature between the high-temperature γ (fcc)

290   phase and the low-temperature ε (hcp) phase is around 970 °C. In pure Co the equilibrium

291   temperature between the two phases is around 427°C [28]. The fcc $\rightarrow$ hcp transformation in Co

292   and its alloys is very sluggish due to the limited chemical driving forces available at the

293   transformation temperature. Thus, under normal cooling conditions, the fcc phase is retained

294   below the phase boundary in a metastable state. The metastable fcc phase can transform to hcp

295   by plastic deformation, by isothermal aging at temperatures between 650 and 950 °C, and

296   athermally, by rapid cooling from the annealing temperatures (> 1100°C) [24,29]. In our

297   samples, the laser beam produces the local melting of the metal powder that rapidly solidifies

298   and cools down due to the high thermal conductivity of the metallic alloy and the smallness of

299   the heated area during the laser treatment. Thus, in the successive small areas treated with the

300   laser beam during the production process is possible to reach a condition very similar to that

301   responsible of the athermal martensitic transformation. Accordingly the athermal martensitic

302   transformation is the origin of the ε (hcp) phase in our sintered samples.

303   SEM observations of the DLMS samples, reveal a complex microstructure. Parallel columnar

304   structures form different domains inside the same melted pool produced by the laser beam. This

305   morphology is very different from the cellular dendritic morphology observed by Meacock et al

306   [17]. They reported on the microstructure and properties of a typical Co-Cr-Mo biomedical alloy

307   manufactured by laser powder microdeposition (LPMD). Although this latter technique,

308   similarly to the DLMS, involves melting of a small quantity of metal powder by a laser beam

309   followed by a rapid quenching, different microstructures are produced. It must be stressed that

310   the laser sintering process is very complex because it involves multiple modes of heat, mass and

311   momentum transfer, and chemical reactions [5]. As a consequence, it is not too surprising that

312   two different laser sintering techniques produce different final samples microstructure. Gaytan et

313   al. [16] reported on the microstructure and mechanical properties of parts fabricated by electron

314   beam melting (EBM) of a Co-26Cr-6Mo-0.2C powder. They observed hardness values similar to

315   the values experimentally obtained in our work, attributed to the formation of carbides lined up

316   to form columns perpendicular to the build direction. Although the columns of carbides look

317   similar to the columnar structures visible in our SEM images, XRD and TEM analyses show that

318   metal carbides are only present in small quantities and do not form columnar structures in our

319   samples. In particular, TEM observations reveal the formation of ε-martensite lamellae inside the

320   fcc-Co grains. These lamellae grow on the {111} planes of the cubic γ-phase and tend to

321   aggregate forming the columnar structures visible in the SEM images. Therefore, the columnar

322   structures visible in our SEM images although similar to other structure reported in literature,

323   have a completely different nature, never observed before.

324   As known, the hcp stacking sequence can be produced by introducing an intrinsic stacking fault

325   on every second (111) plane of an fcc lattice. Furthermore, this can be accomplished by a

326   shearing process if the intrinsic faults are bounded by Shockley a/6 <112> partial dislocations.

327   This mechanism, invoked in the fcc→hcp martensitic transformation [30], explains the

328   orientation relationship between the ε and the γ phases experimentally observed in the electron

329   diffraction patterns reported in Fig. 4b. Considering the different families of {111} planes, the

330 presence of different orientations of the columnar structures inside a single melt pool is not

331 surprising.

332 The estimation of the area fraction occupied by the columnar structures with respect to the

333 matrix, obtained by SEM images elaboration, is comparable with the ε-phase volume fractions

334 obtained by XRD spectra analyses. This is in agreement with TEM observations revealing that

335 the columnar structures are due to the aggregation of ε-martensite lamellae.

336 Generally, for a conventional Co-Cr-Mo alloy, the percentage of athermal ε-martensite ranges

337 from 10 vol.% to 15vol.% depending on the chemical composition of the alloy, the solution

338 temperature and time, and the cooling rate [28]. Using only conventionally [31] or laser sintered

339 [17] Co-Cr-Mo powders, amounts of athermal ε-martensite ranging from 30 vol.% to 70 vol.%

340 were produced. The reason for these large amounts was mainly attributed to a large nucleation of

341 ε-embryos promoted by the free surfaces and grain development at powder contact surfaces

342 combined with recrystallization and grain growth within the powder particles, or promoted by

343 the cell grain boundary between the dendritic and interdendritic zone. In our samples, the cellular

344 dendritic morphology was not observed, and the powder particles completely melted during the

345 laser treatment. Thus, it is not possible to invoke in our samples the same mechanisms of

346 nucleation promotion. Furthermore, in the two above-mentioned works, TEM analyses were not

347 performed, therefore it is not possible to compare the distribution and morphology of the ε-

348 phase. Comparisons can be performed with the athermal ε-martensite present in conventional

349 Co-Cr-Mo alloys [32]. In such case, the ε-phase forms thick bands inside the fcc-phase. To our

350 knowledge, the formation of an intricate network of thin ε-lamellae, comparable to that of our

351 samples, was never observed before. All this suggests that in the DLMS procedure the cooling

352 rates of the melted powder are so rapid that a lot of lattice defects are formed during

353   solidification, and these defects exactly represent the ε-embryos promoting the martensitic

354   transformation.

355   For completeness, during the samples sintering, the deposited layers were heated as each

356   successive layer was deposited. These heating treatments could have induced isothermal

357   martensitic transformations in the alloy. However, it is reported in literature that the isothermal

358   martensitic formation is accompanied by the formation of discontinuous rows of carbides

359   connected to the negligible carbon solubility in the hcp phase [30,33]. The spherical carbides

360   present in our samples do not satisfy the features reported above, and they are probably formed

361   during the solidification process.

362   The HRC hardness values reported for the common cast Co-Cr-Mo alloys range from 25 to 35

363   HRC. These values are considerably lower than those measured in the part manufactured by

364   DLMS. Furthermore, it was found that the hardness value exhibits a linear increase at the

365   increasing of the ε phase content [24]. This latter result can be attributed to the growth of the ε-

366   phase on the $\{111\}_\gamma$ planes that restrict dislocation slip in the fcc lattice. Moreover, the

367   dislocation slip in the hcp lamellae is also inhibited by the intersection of these hcp lamellae with

368   other hcp ones or with fcc regions [30]. Therefore, all the aforementioned phenomena and the

369   peculiar intricate network of ε-lamellae experimentally observed in our samples, can explain the

370   high hardness values obtained. In fact, in our samples the ε lamellae grow on the slip plains of

371   the γ-(fcc) phase. The density and the spatial distribution of these ε lamellae enormously restrict

372   the dislocations slip, thus increasing the hardness values of our samples.

373   The presence of metal carbides could even play a role in the strengthening of the alloy by the

374   Orowan mechanism. However, considering the small quantity of carbides observed in our

375   samples, it is more probable that the main mechanism of strengthening is due to the martensitic

376   transformation induced in the alloy by the DLMS procedure.

377   The increased hardening manifested in the sintered samples along with the microstructure

378   homogeneity observed could make the direct metal laser sintering technique a very useful and

379   powerful procedure to produce surgical implants from Co-Cr-Mo alloys. In this framework, it

380   must be stressed that high hardness values are particularly desirable in the field of prosthesis

381   applications to reduce the debris due to the friction action in the polyethylene-on-metal artificial

382   joints. As shown by Gonzalez-Mora et al. [34], that studied the role of hardness and roughness

383   on the wear of polyethylene in the polyethylene-on-metal artificial joints, hard surfaces are more

384   resistant against scratching and consequently produces less polyethylene wear, the roughness

385   being not the main parameter.

386   Future work will involve studies on the correlation between the deposition parameters of the

387   DMLS production process, and the microstructure and the mechanical properties of the final

388   products. Furthermore, additional mechanical tests will be performed on the sintered Co-Cr-Mo

389   samples in order to investigate tensile strength, Young's modulus and elongation.

390

391   **5. CONCLUSIONS**

392   In the present paper, we reported on the structural and microstructural characterization of Co-Cr-

393   Mo parts produced by Direct Metal Laser Sintering. The composition of the alloy was chosen in

394   order to produce biocompatible parts. Sintered samples were characterized by X-ray diffraction,

395   scanning and transmission electron microscopy and EDS microanalysis. The main results

396   obtained can be listed as follows:

397 1) The laser treatment melts the metallic Co-Cr-Mo powder and induces a phase transformation

398 from the γ (fcc) to the ε (hcp) phase;

399 2) The phase transformation is an athermal martensitic transformation and produces an intricate

400 network of thin ε-lamellae distributed inside the γ phase. This microstructure was never observed

401 before;

402 3) The large amount of ε-lamellae could be attributed to a large nucleation of ε-embryos

403 promoted by lattice defects formation during the rapid cooling of the melted powder;

404 4) Carbides are present inside the grains of the alloy and are probably formed on solidification;

405 5) The hardness values of the samples, higher than those reported in parts fabricated by different

406 processes, are due to the presence of ε-lamellae grown on the $\{111\}_\gamma$ planes that restricts the

407 dislocations slip in the γ (fcc) phase. Furthermore, slip in the ε-lamellae is inhibited by the

408 intersection of these hcp lamellae with other hcp lamellae or with fcc regions.

409 6) The DMLS technique could be used to realize surgical implants, where a high degree of

410 personalisation is required, saving money and time with respect to conventional procedures.

411

414

415 **REFERENCES**

416 [1] A. Mazzoldi. Selective laser sintering in biomedical engineering. Med Biol Eng Comput

417 2013;51:245-256.

418 [2] Lantada AD, Morgado PL. Rapid prototyping for biomedical engineering: current capabilities

419 and challenges. Annual Review of Biomedical Engineering 2012;14:73-96.

420 [3] Rosochowski A, Matuszak A. Rapid tooling: the state of the art. J Mater Process Technol

421 2000;106:191-198.

422 [4] Hunt JA, Callaghan JT, Sutcliffe CJ, Morgan RH, Halford B, Black RA. The design and

423 production of Co-Cr alloy implants with controlled surface topography by CAD-CAM method

424 and their effects on osseointegration. Biomaterials 2005;26:5890-5897.

425 [5] Simchi A. Direct laser sintering of metal powders: Mechanism, kinetics and microstructural

426 features. Mater Sci Eng A 2006;428:148-158.

427 [6] Bassoli E, Gatto A, Iuliano L. Joining mechanisms and mechanical properties of PA

428 composites obtained by selective laser sintering. Rapid Prototyp J 2012;18:100-108.

429 [7] Gibson I, Cheung LK, Chow SP, Cheung WL, Beh SL, Savalani M, Lee SH. The use of rapid

430 prototyping to assist medical applications. Rapid Prototyp J 2006;12:53-58.

431 [8] Wang X, Yan Y, Zhang R. Rapid prototyping as a tool for manufacturing bioartificial livers.

432 Trends in Biotechnology 2007;25:505-513.

433 [9] Butscher A, Bohner M, Hofmann S, Gauckler L, Muller R. Structural and material

434 approaches to bone tissue engineering in powder-based three dimensional printing. Acta

435 Biomaterialia 2011;7:907-920.

436 [10] Atzeni E, Iuliano L, Minetola P, Salmi A. Proposal of an innovative benchmark for

437 accuracy evaluation of dental crown manufacturing. Computers in Biology and Medicine

438 2012;42:548-555.

439 [11] Davis JR. Nickel, Cobalt and Their Alloys Materials Park (OH): ASM

440 INTERNATIONAL;2000.

441 [12] Nasab MB, Hassan MR, Sahari BB. Metallic biomaterials of knee and hip - a review.

442 Trends Biomater. Artif. Organs 2010;24(2):69-82.

443   [13] Malayoglu U, Neville A. Mo and W as alloying elements in Co-based alloy – their effects

444   on erosion – corrosion resistance. Wear 2005;259:219-229.

445   [14] Shin J, Doh J, Kim J. Effect of molybdenum on the microstructure and wear resistance of

446   cobalt-base Stellite hardfacing alloys. Surf Coat Technol 2003;166:117-126.

447   [15] Davis JR, Handbook of Materials for Medical Devices: ASM International; 2003:21-50

448   DOI: 10.1361/hmmd2003p013.

449   [16] Gaytan SM, Murr LE, Martinez E, Martinez JL, Machado BI, Ramirez DA, Medina F,

450   Collins S, Wicher RB. Comparison of Microstructures and Mechanical Properties of Solid and

451   Mesh Cobalt-base Alloy Prototypes Fabricated by Electron Beam Melting. Metall Mater Trans

452   A 2010;41:3216-3227.

453   [17] Meacock CG, Vilar R. Structure and properties of a biomedical Co-Cr-Mo alloy produced

454   by laser powder microdeposition. J Laser Appl 2009;21:88-95.

455   [18] Vandenbroucke B, Kruth JP. Selective laser melting of biocompatible metals for rapid

456   manufacturing of medical parts. Rapid Prototyp J 2007;13:196-203.

457   [19] Averyanova M, Bertrand P, Verquin B. Manufacture of Co-Cr dental crowns and bridges by

458   selective laser Melting technology. Virtual Phys Prototyp 2011;16:179-185.

459   [20] Reclaru L, Ardelean L, Rusu L, Sinescu C. Co-Cr material selection in prosthetic

460   restoration: laser sintering technology. Solid state phenomena 2012;188:412-415.

461   [21] Cotrut CM, Ciucã S, Miculescu F, Antoniac I, Târcolea M, Vrânceanu DM. The influence

462   of classical and modern manufacturing technologies on the properties of metal dental bridge.

463   Key engineering materials 2014;583:163-168.

464 [22] Sanz C, Navas VG. Structural integrity of direct metal laser sintered parts subjected to

465 thermal and finishing treatments. Journal of materials processing technology 2013;213:2126-

466 2136.

467 [23] Saldivar-Garcia AJ, Lopez HF. Temperature effects on the lattice constants and crystal

468 structure of a Co-27Cr-5Mo low-carbon alloy. Metall Mater Trans A 2004;35:2517-2523.

469 [24] Garcia JS, Medrano MA, Rodriguez AS. Formation of hcp martensite during the isothermal

470 aging of an fcc Co-27Cr-5Mo-0.05C orthopedic implant alloy. Metall Mater Trans A

471 1999;30:1177-1184.

472 [25] Rasband WS. ImageJ, U. S. National Institutes of Health, Bethesda, Maryland, USA,

473 http://imagej.nih.gov/ij/ 1997-2012.

474 [26] CrystalKitX version 1.9.1. Total Resolution LLC.

475 [27] Murr LE, Amato KN, Li SJ, Tian YX, Cheng XY, Gaytan SM, Martinez E, Shindo PW,

476 Medina F, Wicker RB. Microstructure and mechanical properties of open-cellular biomaterials

477 prototypes for total knee replacement implants fabricated by electron beam melting. J Mech

478 Behav Biomed Mater 2011;4:1396-1411.

479 [28] Saldìvar-Garcia AJ, Manì MA, Salinas RA. Effect of solution treatments on the fcc/hcp

480 isothermal martensitic transformation in Co-27Cr-5Mo-0.05C aged at 800°C. Scr Mater

481 1999;40:717-722.

482 [29] Lopez HF. Alloy developments in biomedical Co-base alloys for HIP implant applications.

483 Materials science forum 2013;736:133-146.

484 [30] Vander Sande JB, Coke JR, Wulff J. A Transmission Electron Microscopy Study of the

485 Mechanisms of Strengthening in Heat-Treated Co-Cr-Mo-C Alloys. Metall Trans A

486 1976;7A:389-397.

487   [31] Song CB, Park HB, Seong HG, Lòpez HF. Development of a thermal ε-martensite in

488   atomized Co-Cr-Mo-C implant alloy powders. Acta Biomaterialia 2006;2:685-691.

489   [32] Lee SH, Nomura N, Chiba A. Significant improvement in mechanical properties of

490   biomedical Co-Cr-Mo alloys with combination of N addition and Cr-enrichment. Mater Trans

491   2008;49:260-264.

492   [33] Rajan K, Vander Sande JB. Room temperature strengthening mechanisms in a Co-Cr-Mo-C

493   alloy. J Mater Sci 1982;17:769-778.

494   [34] Gonzalez-Mora VA, Hoffmann M, Stroosnijder R, Gil FJ. The role of hardness and

495   roughness on the wear of different CoCrMo counterfaces on UHMWPE for artificial joints. J

496   Biomedical Science and Engineering 2011;4:651-656.